HAL
open science

Comprehensive analysis of electron evaporative cooling in double-barrier semiconductor heterostructures

Marc Bescond, Guillaume Dangoisse, Xiangyu Zhu, Chloé Salhani, Kazuhiko Hirakawa

To cite this version:

Marc Bescond, Guillaume Dangoisse, Xiangyu Zhu, Chloé Salhani, Kazuhiko Hirakawa. Comprehensive analysis of electron evaporative cooling in double-barrier semiconductor heterostructures. Physical Review Applied, 2022, 17 (1), pp.014001. 10.1103/PhysRevApplied.17.014001 . hal-03511340

HAL Id: hal-03511340

https://hal.science/hal-03511340v1

Submitted on 4 Jan 2022

HAL is a multi-disciplinary open access archive for the deposit and dissemination of scientific research documents, whether they are published or not. The documents may come from teaching and research institutions in France or abroad, or from public or private research centers.

L'archive ouverte pluridisciplinaire **HAL**, est destinée au dépôt et à la diffusion de documents scientifiques de niveau recherche, publiés ou non, émanant des établissements d'enseignement et de recherche français ou étrangers, des laboratoires publics ou privés.

Comprehensive analysis of electron evaporative cooling in double-barrier semiconductor heterostructures

Marc Bescond,[1,2,*] Guillaume Dangoisse,[1,2,3] Xiangyu Zhu,[1] Chloé Salhani,[1,2] and Kazuhiko Hirakawa[1,2,4,†]

[1] *Institute of Industrial Science, University of Tokyo, 4-6-1 Komaba, Meguro-ku, Tokyo 153-8505, Japan*
[2] *LIMMS-CNRS, IRL 2820, 4-6-1 Komaba, Meguro-ku, Tokyo 153-8505, Japan*
[3] *Ecole Normale Supérieure de Paris, Université PSL, Sorbonne Université, Université de Paris, 75005 Paris, France*
[4] *Institute for Nano Quantum Information Electronics, University of Tokyo, 4-6-1 Komaba, Meguro-ku, Tokyo 153-8505, Japan*

Based on full quantum transport simulations, we report a comprehensive study of the evaporative cooling process in double-barrier semiconductor heterostructure thermionic refrigerator. Our model, which self-consistently solves the non-equilibrium Green's function framework and the heat equation, is capable to calculate the electron temperature and electrochemical potential inside the device. By investigating the dependence of those thermodynamic parameters as a function of the barrier thickness and height, we answer open questions on evaporative cooling in solid state systems, and give a clear recipe to reach high electron refrigeration. In particular, simulation results demonstrate that the best cooling is obtained when i) the device operates at the maximum resonant condition; ii) the quantum well state is symmetrically coupled with the contacts. The present results then shed light on physical properties of evaporative cooling in semiconductor heterostructures and will allow to speed up the development of thermionic cooling devices towards unprecedented performances.

I. INTRODUCTION

Heat transport at the nanoscale severely limits the scaling of high-performance information and communication systems. In micro/nano-electronics, the drastic increase of chip power consumption generates hot-spots inside the devices[1,2], significantly degrading their performance[3,4]. On the other hand, the cooling approaches of integrated circuits are based on liquid or air (fans) active refrigeration techniques[5], which refrigerate the entire chip and are therefore extremely power consuming. For example, 40% of the energy consumed by data centers is devoted to cooling[6]. In the field of quantum technologies[7], which requires sub-1K temperature, the usual cryo-liquid-based cooling stage is also very cumbersome[8]. The "classical" electronic control module of the quantum bits operates at higher temperature and makes the cooling of the physical system very challenging and energetically dissipative. In those two important fields, the development of efficient electronic nano-refrigerators, which directly target the hot region, represents a major scientific and technological task in a context of energy resource shortage[9,10].

Innovative cooling technologies, emerging from solid-state physics, could overcome those limitations. Recently, thermoelectric devices based on Peltier effect have attracted an increasing interest[11]. Those devices are based on the diffusive phonon and electron transport, and operate in close to equilibrium regime, where their cooling power is obviously limited. The other type of electronic coolers are based on the thermionic junction, which assumes a strong ballistic transport of carriers and which is based on energy filtering of electrons by a potential barrier. The field of thermionic cooling, operating in the non-equilibrium regime, raises the opportunity to obtain higher cooling power and efficiency than in conventional thermoelectric devices[12].

Electronic refrigerators using thermionic cooling were vastly investigated from the 90's with the emergence of semiconductor heterostructures in which quasi-ballistic transport and energy filtering of electrons can occur. This very general concept has been then applied to different physical systems, like in single barrier structure[13], HgCdTe/CdTe heterostructures[14], double-heterojunction structure[15], molecular junctions[16,17], quantum dots[18,19] and NIS (Normal-Insulator-Superconductor) junctions[8,20] . In those refrigerators, the lattice cooling results from the prior refrigeration of the electron system. Indeed, the selective emission of hot electrons induces a so-called evaporative cooling process[21] on the electron gas[22,23]. So far, this effect remains rather unexplored in semiconductor structures due to a lack of theoretical insight. In particular the interplay between barrier height, transport properties and electron temperature is still unclear. Therefore extensive theoretical investigations on evaporative cooling are needed. In order to capture the key aspects of the physics, we use the quantum non-equilibrium Green's function (NEGF) method. Our quantum transport code takes into account the thermal effects by self-consistently coupling the electron transport equations expressed within the NEGF formalism with the heat equation[24,25]. We also use the virtual probe concept to calculate the electron temperature and electrochemical potential inside the device[26,27].

We will focus on double-barrier asymmetric heterostructures since we recently demonstrated that such device can efficiently acts on the electronic bath's refrigeration[28]. We consider the device shown in Figure 1. It illustrates the band diagram of the asymmetric

double-barrier heterostructure which couples "tunnel injection" and "thermionic extraction". In this structure, "cold" electrons are injected from the emitter into the GaAs quantum well (QW) via a resonant tunneling effect through a thin potential barrier (labelled as "emitter barrier"). The role of the emitter barrier is to filter injected electrons and to concentrate the cooling in the QW. "Hot" electrons are removed from the QW through a thermionic process above the thick AlGaAs alloy (labelled as "collector barrier"), extracting energy from the lattice via phonon absorption. Electrons are then relaxed in the collector by emitting phonons. As a result, the QW cools and the collector heats. We showed that electron bath in the QW was also refrigerated thanks to the evaporative cooling effect. When applying a bias, hot electrons are extracted above the thick collector barrier and the remaining low energy ones re-thermalize in the QW at a lower temperature. Electron temperature reduction as high as several tens of Kelvins has been demonstrated both experimentally and theoretically[28]. However, the dependence of the electron temperature on the physical parameters of the device is still not well understood. In particular, it would be very relevant to provide a general recipe to design the configuration offering the best electron cooling.

In this work, we then extensively study of the electron temperature dependence with respect to the emitter barrier thickness (L_{Emit}) and to the activation energy W by varying the height of the collector barrier. For a given structure, we demonstrate that the best electron cooling is reached at the resonant regime, i.e. when the QW state (E_0 in Fig. 1) is aligned with the bottom of the conduction band of the emitter. Varying L_{Emit}, the overall electron temperature minimum is obtained when the QW state is symmetrically coupled to the emitter and collector reservoirs. Finally, the extraction of a larger component of hot electrons through the reduction of W does not induce a better evaporative cooling. This counterintuitive result is due tunnel leakage of the injected electrons through the tilted collector barrier, leading to an increase of the electron temperature.

The paper is organized as follows. Section II describes the electronic quantum transport, heat transport model, and thermodynamic parameters calculation based on the virtual probe approach. In Section III we discuss the influence of L_{Emit} and activation energy W on the electron temperature and electrochemical potential in the QW. From these numerical investigations, we propose general recommendations to reach the most important electron cooling. Finally, Section IV draws our concluding remarks.

II. THEORETICAL APPROACH

In order to theoretically study such a quantum device, we couple both electron and phonon transport.

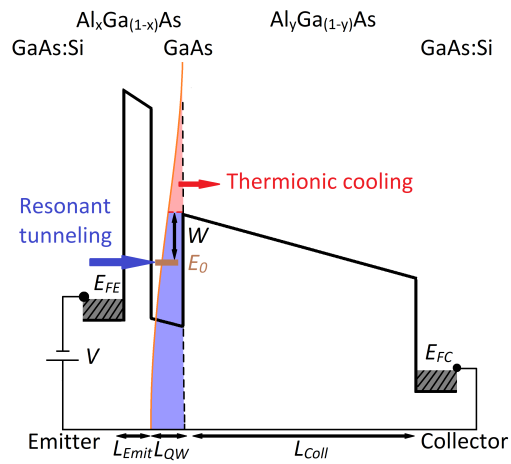

FIG. 1. (Color online) Sketch of the considered asymmetric double-barrier heterostructure. L_{Emit}, L_{QW} and L_{Coll} refer to the thicknesses of the emitter barrier, the quantum well and the collector barrier respectively. W is the activation energy, defining the gap between the QW state E_0 and the top of the collector barrier. E_{FE} and E_{FC} are the Fermi levels of the emitter and collector respectively. For all the considered devices, doping in the emitter and the collector is 10^{18} cm^{-3}, L_{QW}=6 nm and L_{Coll}=100 nm. x and y are the aluminum concentrations in the emitter and collector barrier respectively. x=0.5, corresponding to barrier heights of 0.37 eV while y is a varying parameter.

A. Transport of electron and heat

Electron transport is described via the NEGF quantum formalism[29,30]. Transport equations are expressed within the effective mass approximation to implement a quantum simulator along the heterostructure growth direction (x). The single band effective mass Hamiltonian describes the Γ-valley of the conduction band of the III-V semiconductors. We consider an isotropic energy dispersion in the transverse plane for the conduction band and therefore adopt a cylindrical cross-section. Born-Von-Karman periodic boundary conditions applied on the transverse wave function leads to $\pi(2\times n_{k_t}+1)$ discretized transverse wave vectors k_t given by $k_t = n_{k_t} \times 2\pi/L_t$, with $L_t = 50$ nm is the cylinder diameter and n_{k_t} is an integer[31]. In the following, we summarize the main features of the NEGF approach in matrix notation. We first define the retarded Green's function at the energy E for each transverse mode k_t,

$$G^r_{k_t} = \left[(E-V)I - H_{k_t} - \Sigma^r_{L,k_t} - \Sigma^r_{R,k_t} - \Sigma^r_{S,k_t}\right]^{-1}, \quad (1)$$

where I is the identity matrix, H_{k_t} represents the effective mass Hamiltonian for the transverse mode k_t and V is the electrostatic potential energy. $\Sigma^r_{L/R}$ and Σ^r_S are the retarded self-energies for the left/right semi-infinite de-

TABLE I. Principal NEGF parameters used in this work.

	m^*_Γ(GaAs)	m^*_Γ(AlAs)	m^*_Γ($Al_xGa_{1-x}As$)	$\hbar\omega_{LO}$ (meV)	ϵ_0	ϵ_∞
	0.067	0.15	x.m^*_Γ(AlAs)+(1-x).m^*_Γ(GaAs)	35	12.9	10.89
Ref.	40	40	40	41	41	41

vice contacts[32] and scattering mechanisms, respectively.

From the retarded Green's function, the lesser/greater Green's functions are then obtained as

$$G^{\lessgtr}_{k_t} = G^r_{k_t}\left(\Sigma^{\lessgtr}_{L,k_t} + \Sigma^{\lessgtr}_{R,k_t} + \Sigma^{\lessgtr}_{S,k_t}\right) G^{r\dagger}_{k_t}, \tag{2}$$

where the $\Sigma^{\lessgtr}$ are the lesser/greater self-energies, related to their retarded counterpart by

$$\Sigma^r = \frac{1}{2}\left[\Sigma^> - \Sigma^<\right]. \tag{3}$$

Only acoustic- and polar optical-phonon[33] interactions are considered, since non-polar-optical phonons turn out to be negligible in the semiconductors considered in this work[34]. Polar optical phonons (POP) have an energy $\hbar\omega_{LO}$=35 meV, while interactions with acoustic ones (AC) are assumed elastic at room temperature[35]. Note that electron-electron interactions have been neglected since very few studies reported such scattering treatment in realistic devices. Recently, Urs Aeberhard proposed a relevant approximation to treat this numerically very demanding interaction (see Ref.36). In this work, the author applies the formalism to the case of hot-carrier solar cells and shows that electron-electron interaction was essential to obtain an increase of electron temperature with respect to the lattice temperature. We have implemented this electron-electron interaction in our NEGF code and found that such interaction did not have an impact on the electron temperature in the case of evaporative cooling. From our understanding, the main reason for this negligible effect is due to the small electron density in the quantum well, which goes from 10^{12} m^{-2} to few 10^{14} m^{-2} depending on the applied bias and the emitter barrier thickness. It would be interesting to better investigate the origin of this behavior, but this point goes far beyond the aim of present paper since the incorporation of electron-electron interaction in realistic devices represents a research field in itself.Interaction self-energies are calculated within the self-consistent Born approximation (SCBA)[37–39].

The total phonon scattering SCBA self-energy $\Sigma^{\lessgtr}_{S,k_t}$ for a given mode k_t can be then decomposed as :

$$\Sigma^{\lessgtr}_{S,k_t} = \Sigma^{\lessgtr}_{AC,k_t} + \Sigma^{\lessgtr}_{POP,k_t}. \tag{4}$$

Once the lesser/greater Green's function $G^{\lessgtr}_{k_t}$ of each mode k_t is determined, electron density can be calculated[37]:

$$n_j = -2 \times \frac{i}{2\pi}\sum_{k_t}\pi(2n_{k_t}+1)\int_{-\infty}^{+\infty} G^<_{k_t}(j,j;E)dE, \tag{5}$$

$$= -i\int_{-\infty}^{+\infty} G^<(j,j;E)dE, \tag{6}$$

with $G^<(j,j;E) = \sum_{k_t}(2n_{k_t}+1)G^<_{k_t}(j,j;E)$ and the index j indicates the x position along the discretized domain. The carrier current density flowing from position j to $j+1$ is calculated from the off-diagonal elements $(j,j+1)$ of $G^<_{k_t}(i,j;E)$ as

$$J_{j\to j+1} = \int_{-\infty}^{+\infty} dE\frac{e}{\hbar}\sum_{k_t}\frac{(2n_{k_t}+1)}{S} \left[H_{j,j+1}G^<_{k_t}(j+1,j;E) - G^<_{k_t}(j,j+1;E)H_{j+1,j}\right], = \int_{-\infty}^{+\infty}\mathcal{J}_{j\to j+1}(E)dE. \tag{7}$$

where $H_{j,j+1}$ corresponds to the nearest neighbor hopping term in the discretized tight-binding like Hamiltonian and $\mathcal{J}_{j\to j+1}(E)$ is the current density spectrum (in A/(m$^2\cdot$ eV)). From Eq.(7) we can deduce the corresponding electronic energy current[42]:

$$J^E_{j\to j+1} = \int_{-\infty}^{+\infty} E\mathcal{J}_{j\to j+1}(E)dE. \tag{8}$$

In practice, the set of Eqs. (1)-(4) is solved self-consistently using a recursive algorithm[32,43] until the criteria of convergence for both electron density and carrier current density are reached. The potential energy V is self-consistently determined by nonlinearly coupling the transport equations (1)-(4) with the Poisson equation through the electron density. In all the study, band offsets are calculated based on the values reported in Ref.40. The other parameters used in the NEGF code are reported in Table I.

The derivative of Eq. (8) directly determines the energy transferred between the electron bath and the lattice, establishing the coupling between the heat equation and electron transport equations. The 1D heat equation along the x direction is then iteratively solved together

with the transport equations and the Poisson equation, until a global self-consistency is achieved. This approach has been precisely described in Ref.24 and 25.

B. Electron temperature

Since the device operates in a strongly non-equilibrium regime, temperature of electrons can significantly differ from its lattice counterpart. In this section, we calculate the local electronic temperature based on the virtual probe approach. Such a method can determine the local electronic temperature and electrochemical potential by cancelling the particle and energy currents between a floating probe and the device. The probe is then in local thermodynamic equilibrium with the non-equilibrium structure. Stafford and co-workers[26,27,44] showed that temperature and electrochemical potential determined within this approach are physically-consistent, as they are unique and fulfill the four laws of thermodynamics.

We then consider a thermoelectric probe at the position j along the x-axis defined by the following self-energy (similar to the Büttiker probes[45–47]):

$$\Sigma^{>}(j;E) = -i[1 - f_{FD}(E,\mu_j,T_j^e)]LDOS(j;E)\nu_{coup}, \tag{9}$$

$$\Sigma^{<}(j;E) = i f_{FD}(E,\mu_j,T_j^e)LDOS(j;E)\nu_{coup}, \tag{10}$$

where f_{FD} is the Fermi-Dirac distribution of the electrons in the probe, μ_j and T_j^e are respectively the local electrochemical potential and electronic temperature at the position j; $LDOS(j;E) = i\frac{[G^{>}(j,j;E)-G^{<}(j,j;E)]}{2\pi}$ is the local density of states of the probe (taken equal to the one of the device) and ν_{coup} is the energy independent coupling strength between the probe and the system. In the considered case, the exact value of ν_{coup} is not important, as it will cancel out in the following computations.

By enforcing the simultaneous cancellation of the electron charge and energy currents between the device and the probe, we obtain a system of two coupled nonlinear equations in the unknowns μ_j and T_j^e:

$$\Delta J(j) = \int_{-\infty}^{+\infty} \Sigma^{>}(j;E)G^{<}(j,j;E)dE - \int_{-\infty}^{+\infty} G^{>}(j,j;E)\Sigma^{<}(j;E)dE = 0, \tag{11}$$

$$\Delta J^E(j) = \int_{-\infty}^{+\infty} E\Sigma^{>}(j;E)G^{<}(j,j;E)dE - \int_{-\infty}^{+\infty} EG^{>}(j,j;E)\Sigma^{<}(j;E)dE = 0. \tag{12}$$

The system is iteratively solved at each position j through a Newton-Raphson algorithm[48]. Finally, we calculate the weighted average of μ and T^e in the QW with respect to the electron density as follows:

$$T_{QW}^e = \sum_{j\in QW} \frac{T_j^e \times n_j}{\sum_{i\in QW} n_i}, \tag{13}$$

$$\mu_{QW} = \sum_{j\in QW} \frac{\mu_j \times n_j}{\sum_{i\in TOT} n_i}. \tag{14}$$

These calculations are done as a post-processing step once the self-consistent lesser and greater Green's functions of the system are obtained.

III. RESULTS AND DISCUSSION

A. Physical analysis

In this section we analyze the dependence of the electron cooling in the quantum well with respect to L_{Emit} and the height of the collector barrier. We first consider the structure shown in Fig. 1 with L_{Emit}=6 nm and y=0.25 (aluminum content), which corresponds to a collector barrier height of 0.21 eV. Figure 2 shows the calculated current-voltage characteristics given by the quantum transport simulations and obtained from experimental measurements. The samples were grown on n-type GaAs substrates by using molecular beam epitaxy. We successively grew a 300 nm-thick n^+-GaAs emitter layer (Si doping density = 1×10^{18} cm^{-3}), a 5 nm-thick undoped GaAs spacer layer, an undoped 6 nm-thick $Al_{0.5}Ga_{0.5}As$ emitter barrier, an undoped 6 nm-thick GaAs QW, an undoped 100 nm-thick $Al_{0.25}GaAs_{0.75}As$ collector barrier, and a 200 nm-thick n^+-GaAs collector layer (Si doping density = 1×10^{18} cm^{-3}). The wafer was then photolithographically patterned into mesa structures with various areas ranging from 80×80 μm^2 to 800×800 μm^2. AuGeNi/Au contacts were deposited on the front and back sides. The samples were finally annealed at 450 °C in Ar ambient for 5 s.

Since no adjusting parameter has been used, one can conclude that simulations and experimental results shown in Fig. 2 are in very good agreement. The fact that the peaks in calculations and measurements do not appear at the same bias result from additional series resistance in the experimental set up. However, for the sake of clarity, we decided to show the raw data without any rescaling parameter. The peaks observed at 0.45 V and 0.85 V in the calculations and measurements respectively correspond to the resonant configuration where the

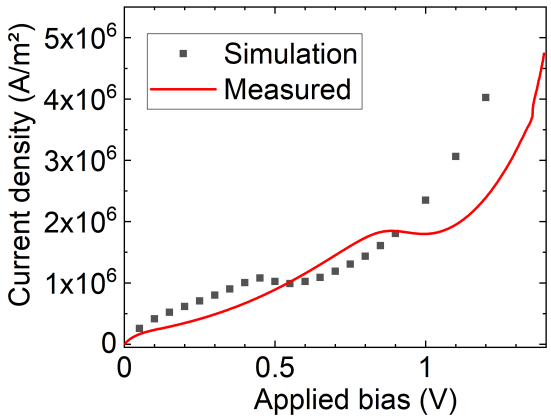

FIG. 2. (Color online) Calculated (squares) and measured (solid line) current-voltage characteristics of the asymmetric double-barrier heterostructure shown in Figure 1. The emitter barrier thickness is L_{Emit}=6 nm and the aluminum concentration in the collector barrier is y=0.25, corresponding to a barrier height of 0.21 eV.

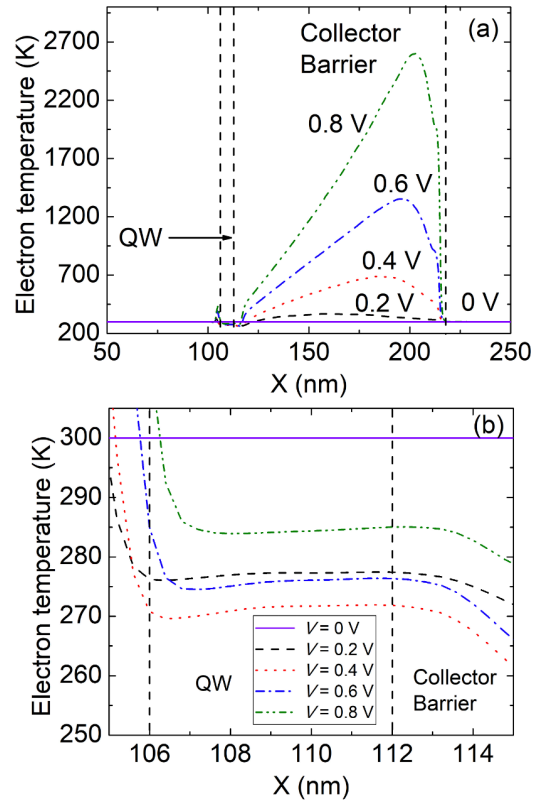

FIG. 3. (Color online) (a) Electronic temperature along the device of Figure 2 obtained for an applied bias varying from 0 V to 0.8 V; (b) Close up of the electron temperature in the QW.

QW state E_0 is aligned with the bottom of the conduction band of the emitter. Increasing the bias, E_0 goes down and electron injection via resonant tunneling requires additional inelastic scattering events. It results in a negative differential resistance. At even larger the bias, the transport mainly relies on direct tunneling across the emitter barrier, and through/above the collector barrier: the current increases again.

Figure 3(a) shows the electron temperature, obtained from the Büttiker probe approach, along the device considered in Figure 2 for an applied bias varying from 0 V to 0.8 V. We first see that the electron temperature is constant equal to 300 K at 0 V, which strengthens the reliability of the floating probe technique. Electron temperature then strongly increases with the applied bias in the collector barrier due to high electric field in this region. On the other hand, the temperature in the QW decreases. Figure 3(b) shows a close up of the temperature in the QW. The temperature is indeed reduced down to 270 K at V=0.4 V. We also note that the temperature is rather constant, even at high bias, since electron density almost vanishes at the edges of the QW.

From those previous results, Figure 4(a) shows the electron temperatures in the QW (Eq. (13)) as a function of the applied bias V for L_{Emit} varying from 1 nm to 6 nm. Temperature depicts similar profile for the six considered thicknesses. Starting from room temperature at equilibrium, it reaches a minimum before sharply increasing above 300 K at large bias. However, the bias corresponding to the temperature minimum varies with L_{Emit}. The red circles of Figure 4(a) indicate the bias at which the resonant condition is fulfilled for each L_{Emit}. Interestingly, we see that the temperature minimum coincides very well with the resonance condition. Indeed, current density being maximum at the resonant regime, the filtering of electrons on the collector barrier is the most important. Beyond the resonance, ballistic electrons are injected into the QW at higher energy, leading to a strong temperature increase.

Figure 4(a) also shows that the temperature reduction increases with L_{Emit}. To shed light on this behavior, Figure 4(b) shows μ_{QW}, the electrochemical potential in the quantum well (Eq. (14)), for the same structures as Figure 4(a). For thin L_{Emit} ($\leqslant$4 nm), the QW is more coupled to the emitter than the collector, and μ_{QW} remains close to the Fermi level of the emitter (E_{FE}). As a consequence, the bias essentially drops in the collector barrier, shifting the resonance (indicated in red circles) towards larger voltages. In that high bias range, the direct tunneling current across the first emitter barrier becomes non-negligible and ballistic high-energy electrons are injected into the QW, leading to a temperature increase.

For thicker L_{Emit}, the couplings between the QW and the two reservoirs become progressively more symmetric.

As such, μ_{QW} is getting closer to the average of the Fermi levels of the emitter (E_{FE}) and collector (E_{FC}), noted E_{FA} ($=(E_{FE}+E_{FC})/2$) in Figure 4(b). The resonance occurs at lower applied bias and thermionic emission now operates on most of the electrons in the QW, leading to the lowest temperatures. We should also note that the decrease of μ_{QW} with the bias accelerates after the resonance since the QW state is not directly coupled to the states of the emitter.

This analysis is also confirmed by the current-voltage characteristics (J-V) shown in Figure 4(c). For thin L_{Emit} ($\leqslant$3 nm), J-V characteristics do not show a negative differential resistance at the resonance (indicated by red circles) due to direct tunneling component across the emitter barrier. On the other hand, the current peak at the resonance becomes more visible as L_{Emit} increases. The current density is also reduced by one order of magnitude, testifying that the emitter barrier resistance increases and that the direct tunneling component is suppressed. Effect of the direct current component will be discussed in more detail in Figure 6.

We now study the influence of L_{Emit} when reducing the height of the collector barrier. We take y=0.15 (aluminum concentration), which corresponds to a collector barrier of 0.11 eV. Intuitively, such a barrier reduction should decrease the activation energy W and amplify the cut-off of the high-energy tail of the distribution of electrons in the QW, inducing lower temperatures.

Figure 5(a) shows the electron temperatures as a function of applied bias V, for the same values of L_{Emit}. Interestingly, the minimum of the electron temperature does not coincide anymore with the bias of resonance (indicated by red circles). Moreover, the minimum of temperature does not monotonously decreases when increasing L_{Emit}. This minimum goes from 285 K for L_{Emit}=1 nm down to 272 K at L_{Emit}=4 nm and increases again up to 280 K for L_{Emit}=6 nm.

To shed light on this latter behavior, Figure 5(b) shows the corresponding electrochemical potentials in the QW. We see that μ_{QW} crossed the average Fermi level E_{FA} for L_{Emit}=5 nm and 6 nm, for which the minimum of temperature increases. In these two cases, the resistance of the collector barrier (R_{Coll}) becomes lower than the resistance of the emitter barrier (R_{Emit}). The resonance then occurs at very low bias, in a near equilibrium regime, where the evaporative cooling process is less efficient. As a result, the temperature minimum increases.

The relative large value of R_{Emit} with respect to R_{Coll} is also visible on Figure 5(c), which shows the corresponding J-V characteristics. For the present collector barrier (y=0.15), the negative differential resistance appears from L_{Emit}=2 nm whereas it was only visible from L_{Emit}>3 nm for y=0.25 (Figure 4(c)). We can also see that the current density decrease is noticeable as soon as L_{Emit} increases, whereas it was limited up to L_{Emit}=5 nm in the case of y=0.25. L_{Emit} and therefore R_{Emit} are clearly the determining parameter.

The reason why resonant state does not provide the best electronic cooling originates from the direct current component, previously discussed. Indeed, we show on Figure 6(a) the current spectrum obtained at the resonance with L_{Emit}=1 nm. For this thin width, the resonance occurs at high bias (V= 1.55 V), since most of bias drops in the collector barrier. The collector barrier has a triangular shape (and a small height since y=0.15) and

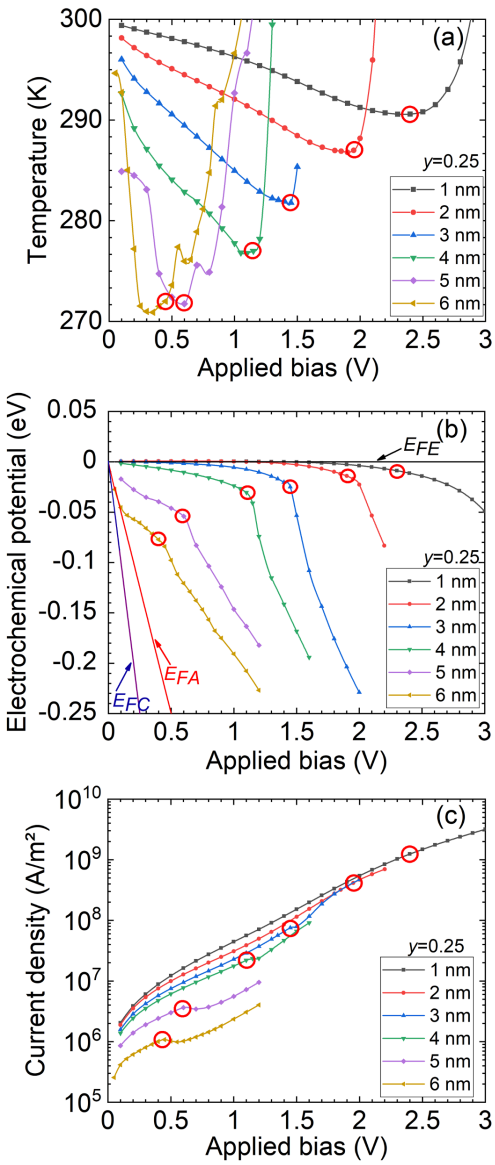

FIG. 4. (Color online) Emitter barrier thickness dependence as a function of the applied bias V for (a) the electron temperature in the QW - Note that for all the devices, temperature exactly equals 300 K at V= 0 V; (b) the electrochemical potential in the QW; (c) the current density. L_{Emit} varies from 1 nm to 6 nm. For each L_{Emit}, red circle represents the bias at which the resonance occurs. We also represent in (b) the Fermi levels of the emitter (E_{FE}), the collector (E_{FC}) and the average of the two ($E_{FA}=(E_{FE}+E_{FC})/2$). Aluminum concentration in the collector barrier is y=0.25, corresponding to a barrier height of 0.21 eV.

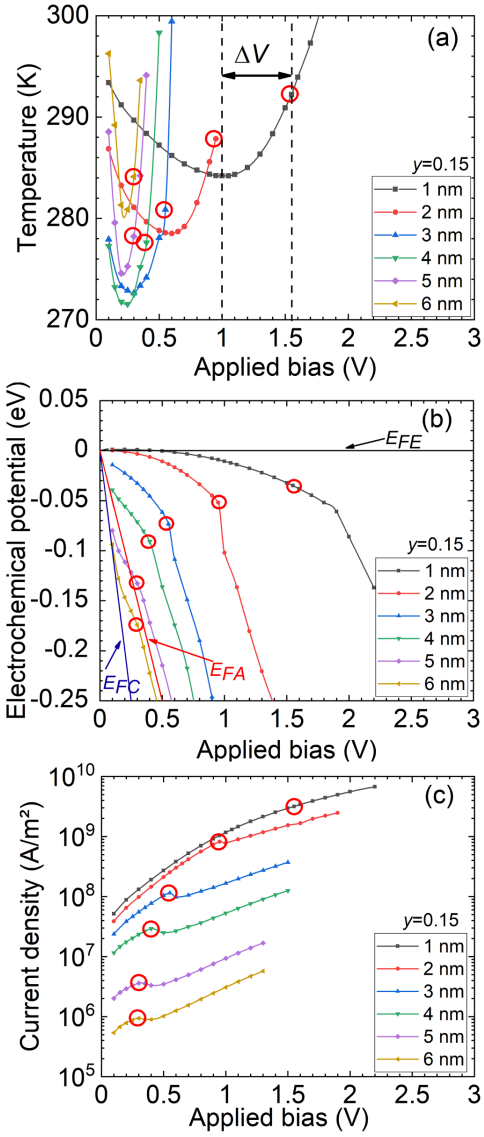

FIG. 5. (Color online) Same as Figure 4 but for an aluminum concentration in the collector barrier y=0.15, corresponding to a barrier height of 0.11 eV.

electrons can easily tunnel though it (see red horizontal arrows). The QW is therefore populated by an important proportion of ballistic high-energy carriers, leading to an increase of temperature. On the opposite, Figure 6(b) shows the current spectrum at the resonance with L_{Emit}=6 nm. At this thickness, most of the applied bias drops on the emitter barrier and the resonance occurs at much lower bias (V= 0.3 V). We clearly see the two components of the resonant tunneling and the thermionic process, which generates the evaporative cooling effect (red arrows).

To confirm this interpretation, we note ΔV the difference between the bias at the resonant state and the one of the temperature minimum (represented in Figure

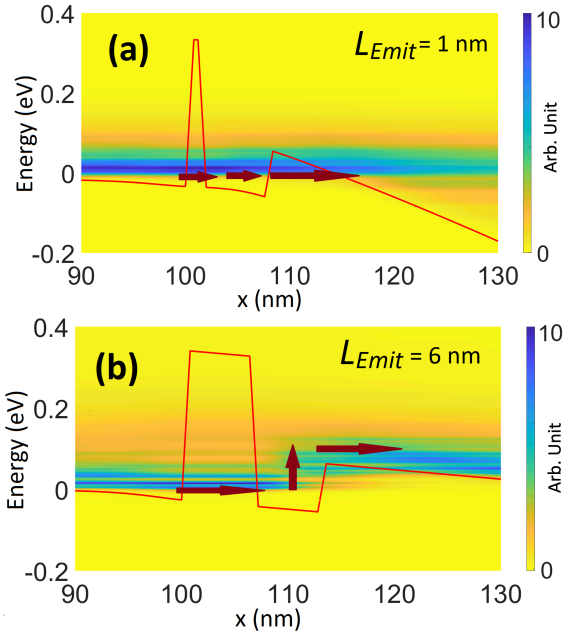

FIG. 6. (Color online) Current spectra at the resonant state for a) L_{Emit}=1 nm (V= 1.55 V) and b) L_{Emit}=6 nm (V=0.3 V). The solid red lines represent the energy potential profile while red arrows indicate the electron flux through and above the collector barrier. Aluminum concentration y=0.15 which corresponds to a barrier of 0.11 eV.

5(a) for L_{Emit}=1 nm). Figure 7 shows the dependence of ΔV with respect to L_{Emit} for y=0.15 and y=0.25. It clearly indicates a ΔV decrease at thick L_{Emit} in the case of a small collector barrier (y=0.15) while ΔV remains rather constant and small for a higher collector barrier (y=0.25). Therefore, for small activation energy and thin L_{Emit}, the resonance occurs at high bias, where the collector barrier becomes partially transparent. It results the injection of ballistic high-energy electrons in the QW and the resonant state does not provide anymore the lowest temperature.

Previous results can be summarized as follows. For a given L_{Emit}, the highest electron cooling is usually reached at the resonant state. When varying L_{Emit}, the overall lowest electron temperature is obtained when the resistance of the emitter barrier is roughly equal to (in fact a bit smaller than) the resistance of the collector barrier. For R_{Emit}<<R_{Coll} the resonance takes place at high applied bias and the injection of ballistic high-energy electrons by direct tunneling impedes the cooling. When R_{Emit}>R_{Coll}, the resonant state occurs at very small applied bias, where the evaporative cooling process can not effectively operate. Moreover a small activation energy does not necessarily improve the cooling properties. It promotes the direct tunneling of ballistic high-energy electrons across the collector barrier, increasing the temperature.

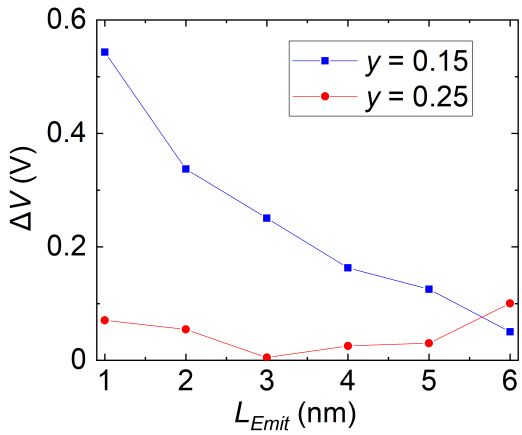

FIG. 7. (Color online) Difference between the voltage of the resonance and the one providing the lowest electron temperature as a function of L_{Emit}. ΔV is also illustrated in Figure 5(a) for L_{Emit}=1 nm. Two aluminum concentrations are considered: y=0.15 (squares) and y=0.25 (circles).

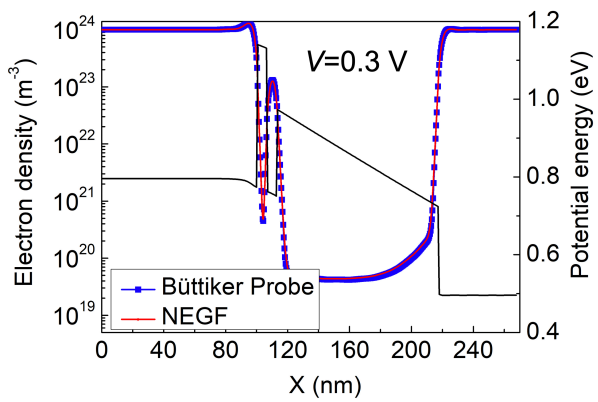

FIG. 8. (Color online) Electron density along the device of Figure 2 at V= 0.3 V, obtained by solving the NEGF transport equations (red solid line), and from equation (15) (blue squares). The conduction band edge is plotted for reference in black solid line.

B. Validity of the virtual probe method

The concept of temperature in strongly non equilibrium systems is an open question in the field of quantum transport. However, several papers recently demonstrated the relevancy of the Büttiker probe concept to determine the carrier temperature[26,27,44,49,50]. Even in the extreme non-equilibrium regime of elastic quantum transport, where electron and phonon baths are completely decoupled, those previous articles demonstrated that an electron temperature and electrochemical potential measured by a floating probe can be interpreted as the local temperature of a non-equilibrium electron system and are physically-consistent, as they are unique and fulfill the four laws of thermodynamics. More precisely, temperature and electrochemical potential are completely determined when the probe-system coupling is: (i) maximally localized, to provide a good spatial resolution, (ii) weak enough to generate a non-invasive measurement, (iii) broadband, to ensure that the measured physical properties depend on the energy spectrum of the structure and not on the one of the probe. In that configuration, the measurement of a temperature of a system far from equilibrium is much more than a simple operational determination of the local temperature. Those findings make a significant step forward to interpret the temperature measured by a floating probe as the local temperature of a non-equilibrium electron system.

In order to validate this approach of measurement of the electronic temperature and electrochemical potential in non-equilibrium regime, we used them for the calculation of the electron density inside the device, considering the following equilibrium electron density expression:

$$n_j^{Probe} = \int_{-\infty}^{+\infty} LDOS(j;E) f_{FD}(E,\mu_j,T_j^e) dE. \quad (15)$$

We then compared the electron density obtained with Eq. (15) and the one obtained through the NEGF approach (Eq.(6)). The figure 8 shows the result of this comparison in the case of the device considered in Figure 2 of the manuscript for an applied potential V = 0.3 V.

The excellent agreement between the two computational approaches definitely supports the physical meaning of of T_e and μ calculated with the floating probe approach.

IV. CONCLUSIONS

In this work, we provided a theoretical comprehensive understanding of the evaporative cooling process in asymmetric double-barrier thermionic device. By varying L_{Emit}, we first demonstrated that the electron cooling is maximum i) at the resonance state and ii) for R_{Emit}≈R_{Coll}. In such condition, a temperature reduction of several tens of kelvins can be reached, irrespective of the barrier resistance value. Of course small resistance, i.e. high current density, will be targeted for an efficient lattice cooling perspective. Moreover, the reduction of the activation energy does not necessarily improve the cooling properties. Indeed it generates the injection in the QW of high-energy electrons which are transmitted across the collector barrier, increasing the electron temperature. In that situation, the temperature minimum occurs before the resonant state. The present paper provides a clear understanding of the evaporative cooling process in room temperature heterostructures and gives a simple recipe to reach the maximum electronic refrigeration. It then represents an important step for the conception, fabrication and optimization of thermionic cooling devices with unprecedented performances. However, it is true that the device shows good electron cooling but a rather weak reduction of lattice temperature. The

physical origin of such a different cooling behavior is due to the huge difference between the heat capacitances of electrons and phonons. A simple solution to improve the phonon system cooling would be to have more electrons in the QW. In our GaAs-based devices, there are typically a few 10^{10} cm^{-2} electrons. An increase in the QW population by several orders of magnitude can be reached by doping or by considering metal/semiconductor junction. Finally, the study of electron refrigeration has applicative interest by itself. In particular, electron cooling may be useful to improve performance of optical devices, such as light emitting devices and photodetectors. For light emitting devices, the reduction in electron temperature leads to narrower linewidth and better luminescence efficiency. As for the photodetectors, it may reduce dark current.

V. ACKNOWLEDGEMENT

We thank G. Bastard for fruitful discussion about the activation energy influence on electron temperature. This work was supported by the JSPS KAKENHI (JP 19K21957), the JSPS Core-to-Core Program (A. Advanced Research Networks) and the GELATO project from ANR (ANR-21-CE50-0017).

* bescond@iis.u-tokyo.ac.jp
† hirakawa@iis.u-tokyo.ac.jp

[1] R. Gaska, A. Osinsky, J. W. Yang, and M.S. Shur, "Self-heating in high-power AlGaN-GaN HFETs," IEEE Electron Dev. Lett. **19**, 89 (1998).
[2] E. Pop and K. E. Goodson, "Thermal phenomena in nanoscale transistors," J. Electron Packaging **128**, 102 (2006).
[3] Reto Rhyner and Mathieu Luisier, "Minimizing self-heating and heat dissipation in ultrascaled nanowire transistors," Nano Lett. **16**, 1022–1026 (2016).
[4] Jayanth Srinivasan, Sarita V Adve, Pradip Bose, and Jude A Rivers, "The impact of technology scaling on lifetime reliability," in *Dependable Systems and Networks, 2004 International Conference on* (IEEE, 2004) pp. 177–186.
[5] S. G. Kandlikar, "Review and projections of integrated cooling systems for three-dimensional integrated circuits," J. Electron. Packag. **136**, 024001 (2014).
[6] M. Avgerinou, P. Bertoldi, and L. Castellazzi, "Trends in data centre energy consumption under the european code of conduct for data centre energy efficiency," Energies **10**, 1470 (2017).
[7] J. P. Dowling and G. J. Milburn, "Quantum technology: the second quantum revolution," Phil. Trans. R. Soc. A **361**, 3655 (2003).
[8] E. Mykknen, J. S. Lehtinen, L. Grönberg, A. Shchepetov, A. V. Timofeev, D. Gunnarsson, A. Kemppinen, A. J. Manninen, and M. Prunnila, "Thermionic junction devices utilizing phonon blocking," Sci. Adv. **6**, eaax9191 (2020).
[9] G. I. Meijer, "Cooling energy-hungry data centers," Science **328**, 318 (2010).
[10] C. Wang, C.-Y. Li, M. P. Hasselbeck, B. Imangholi, and M. Sheik-Bahae, "Precision, all-optical measurement of external quantum efficiency in semiconductors," J. Appl. Phys. **109**, 093108 (2011).
[11] G. Pennelli, "Review of nanostructured devices for thermoelectric applications," Beilstein J. Nanotechnol. **5**, 1268 (2014).
[12] A. Ziabari, M. Zebarjadi, D. Vashaee, and A. Shakouri, "Nanoscale solid-state cooling: a review," Rep. Prog. Phys. **79**, 095901 (2016).
[13] G. D. Mahan, "Thermionic refrigeration," J. Appl. Phys. **76**, 4362 (1994).
[14] A. Shakouri and J. E. Bowers, "Heterostructure integrated thermionic coolers," Appl. Phys. Lett. **71**, 1234 (1997).
[15] T. Zeng and G. Chen, "Interplay between thermoelectric and thermionic effects in heterostructures," J. Appl. Phys. **92**, 3152 (2002).
[16] L. Cui, R. Miao, K. Wang, D. Thompson, L. A. Zotti, J. C. Cuevas, E. Meyhofer, and P. Reddy, "Peltier cooling in molecular junctions," Nat. Nanotechnol. **13**, 122 (2018).
[17] N. Mosso, U. Drechsler, F. Menges, P. Nirmalraj, S. Karg, H. Riel, and B. Gotsmann, "Heat transport through atomic contacts," Nat. Nanotechnol. **12**, 430 (2017).
[18] J. R. Prance, C. G. Smith, J. P. Griffiths, S. J. Chorley, D. Anderson, G. A. C. Jones, I. Farrer, and D. A. Ritchie, "Electronic refrigeration of a two-dimensional electron gas," Phys. Rev. Lett. **102**, 146602 (2009).
[19] A. V. Feshchenko, J. V. Koski, and J. P. Pekola, "Experimental realization of a coulomb blockade refrigerator," Phys. Rev. B **90**, 201407 (R) (2014).
[20] J. T. Muhonen, M. Meschke, and J. P. Pekola, "Micrometre-scale refrigerators," Rep. Prog. Phys. **75**, 046501 (2012).
[21] M. H. Anderson, J. R. Ensher, C. E. Wieman M. R. Matthews, and E. A. Cornell, "Observation of bose-einstein condensation in a dilute atomic vapor," Science **269**, 198 (1995).
[22] T. Jayasekera, K. Mullen, and M. A. Morrison, "Cooling electrons in semiconductor devices: a model of evaporative emission," Phys. Rev. B **75**, 035316 (2007).
[23] D. Suchet, Z. Jehl, Y. Okada, and J.-F. Guillemoles, "Influence of hot-carrier extraction from a photovoltaic absorber: an evaporative approach," Phys. Rev. Appl. **8**, 034030 (2017).
[24] M. Bescond, D. Logoteta, F. Michelini, N. Cavassilas, T. Yan, A. Yangui, M. Lannoo, and K. Hirakawa, "Thermionic cooling devices based on resonant-tunneling AlGaAs/GaAs heterostructure," J. Phys.: Condens. Matter **30**, 064005 (2018).
[25] M. Bescond and K. Hirakawa, "High-performance thermionic cooling devices based on tilted-barrier semiconductor heterostructures," Phys. Rev. Appl. **14**, 064022 (2020).
[26] C. A. Stafford, "Local temperature of an interacting quantum system far from equilibrium," Phys. Rev. B **93**, 245403 (2016).

[27] A. Shastry and C. A. Stafford, "Temperature and voltage measurement in quantum systems far from equilibrium," Phys. Rev. B **94**, 155433 (2016).

[28] A. Yangui, M. Bescond, T. Yan, N. Nagai, and K. Hirakawa, "Evaporative electron cooling in asymmetric double barrier semiconductor heterostructures," Nat. Commun. **10**, 4504 (2019).

[29] S. Datta, *Electronic Transport in Mesoscopic Systems* (Cambridge University Press, Cambridge, U.K., 1995).

[30] H. Haug and A.-P. Jauho, *Quantum Kinetics in Transport and Optics of Semiconductors, vol. 123 of Springer Series in Solid-State Sciences* (Springer, Berlin, New York, 1996).

[31] N. Cavassilas, F. Michelini, and M. Bescond, "Modeling of nanoscale solar cells: The Green's function formalism," J. of Renewable and Sustainable Energy **6**, 011203 (2014).

[32] D. K. Ferry and S. M. Goodnick, *Transport in Nanostructures* (Cambridge University Press, Cambridge, U.K., 1997).

[33] M. Moussavou, M. Lannoo, N. Cavassilas, D. Logoteta, and M. Bescond, "Physically based diagonal treatment of polar optical phonon self-energy: performance assessment of III-V double-gate transistors," Phys. Rev. Appl. **10**, 064023 (2018).

[34] A. Price and A. Martinez, "Electrothermal simulations of Si and III-V nanowire field effect transistors: A non-equilibrium Green's function study," J. Appl. Phys. **12**, 6670 (2015).

[35] M. Bescond, H. Carrillo-Nuez, S. Berrada, N. Cavassilas, and M. Lannoo, "Size and temperature dependence of the electronphonon scattering by donors in nanowire transistors," Solid State Electron. **122**, 1 (2016).

[36] U. Aeberhard, "Quantum transport simulation of hot carrier photocurrent generation in quantum well solar cells," in *Proc. of the 46th Photovoltaic Specialists Conference (PVSC)* (IEEE, 2019) pp. 1729 –1733.

[37] S. Jin, Y. J. Park, and H. S. Min, "A three-dimensional simulation of quantum transport in silicon nanowire transistor in the presence of electron-phonon interactions," J. Appl. phys. **99**, 123719 (2006).

[38] Y. Lee, M. Lannoo, N. Cavassilas, M. Luisier, and M. Bescond, "Efficient quantum modeling of inelastic interactions in nanodevices," Phys. Rev. B **93**, 205411 (2016).

[39] A. Svizhenko and M. P. Anantram, "Role of scattering in nanotransistors," IEEE-Trans. Electron Dev. **50**, 1459 (2003).

[40] I. Vurgaftman, J. R. Meyer, and L. R. Ram-Mohan, "Band parameters for III-V compound semiconductors and their alloys," J. Appl. Phys. **89**, 5815 (2001).

[41] M. S. Lundstrom, *Fundamentals of Carrier Transport* (Cambridge University Press, Cambridge, U.K., 2009).

[42] R. Lake and S. Datta, "Energy balance and heat exchange in mesoscopic systems," Phys. Rev. B **117**, 164501 (1992).

[43] M. Lopez-Sancho, J. Lopez-Sancho, and J. Rubio, "Quick iterative scheme for the calculation of transfer matrices: application to Mo (100)," J. Phys. F: Met. **14**, 1205 (1984).

[44] J. Meair, J. P. Bergfield, C. A. Stafford, and Ph. Jacquod, "Local temperature of out-of-equilibrium quantum electron systems," Phys. Rev. B **90**, 035407 (2014).

[45] M. Büttiker, "Role of quantum coherence in series resistors," Phys. Rev. B **33**, 3020 (1986).

[46] G. Romano, A. Gagliardi, A. Pecchia, and A. Di Carlo, "Heating and cooling mechanisms in single-molecule junctions," Phys. Rev. B **81**, 115438 (2010).

[47] R. Rhyner and M. Luisier, "Atomistic modeling of coupled electron-phonon transport in nanowire transistors," Phys. Rev. B **89**, 235311 (2014).

[48] R. Venugopal, M. Paulsson, S. Goasguen, S. Datta, and M. S. Lundstrom, "A simple quantum mechanical treatment of scattering in nanoscale transistors," J. Appl. Phys. **93**, 5613 (2003).

[49] Y. Dubi and M. Di Ventra, "Reconstructing fouriers law from disorder in quantum wires," Phys. Rev. B **79**, 115415 (2009).

[50] J. P. Bergfield, M. A. Ratner, C. A. Stafford, , and M. Di Ventra, "Local temperature of out-of-equilibrium quantum electron systems," Phys. Rev. B **91**, 125407 (2015).